Graphene-engineered automated sprayed mesoscopic structure for perovskite device scaling-up

To cite this article: Babak Taheri *et al* 2018 *2D Mater.* **5** 045034

2D Materials

RECEIVED
1 June 2018

REVISED
23 July 2018

ACCEPTED FOR PUBLICATION
10 August 2018

PUBLISHED
25 September 2018

PAPER

Graphene-engineered automated sprayed mesoscopic structure for perovskite device scaling-up

Babak Taheri[1], Narges Yaghoobi Nia[1], Antonio Agresti[1], Sara Pescetelli[1], Claudio Ciceroni[1], Antonio Esaù Del Rio Castillo[2], Lucio Cinà[3], Sebastiano Bellani[2], Francesco Bonaccorso[2,4] and Aldo Di Carlo[1,5]

[1] Department of Electronic Engineering, CHOSE—Centre for Hybrid and Organic Solar Energy, University of Rome Tor Vergata, via del Politecnico 1, 00133, Rome, Italy
[2] Graphene Labs, Istituto Italiano di Tecnologia, via Morego 30, 16163 Genoa, Italy
[3] CICCI RESEARCH S.R.L., Grosseto, Italy
[4] BeDimensional Srl., Via Albisola 121, 16163 Genova, Italy
[5] Department of Semiconductor Electronics and Device Physics, National University of Science and Technology 'MISiS', Leninskiy pr.4, Moscow 119049, Russia

E-mail: aldo.dicarlo@uniroma2.it, Francesco.Bonaccorso@iit.it and antonio.agresti@uniroma2.it

Keywords: automated spray coating, perovskite solar cell, graphene, mesoporous TiO_2, 2D material interface engineering

Supplementary material for this article is available online

Abstract

One of the most thrilling developments in the photovoltaic field over recent years has been the use of organic–inorganic lead halide perovskite, such as $CH_3NH_3PbI_3$ ($MAPbI_3$), as a promising new material for low-cost and highly efficient solar cells. Despite the impressive power conversion efficiency (PCE) exceeding 22% demonstrated on lab-scale devices, large-area material deposition procedures and automatized device fabrication protocols are still challenging to achieve high-throughput serial manufacturing of modules and panels. In this work, we demonstrate that spray coating is an effective technique for the production of mesoscopic small- and large-area perovskite solar cells (PSCs). In particular, we report a sprayed graphene-doped mesoporous TiO_2 ($mTiO_2$) scaffold for mesoscopic PSCs. By successfully combining the spray coating technique with the insertion of graphene additive into the sprayed $mTiO_2$ scaffold, a uniform film deposition and a significant enhancement of the electron transport/injection at the $mTiO_2$/perovskite electrode is achieved. The use of graphene flakes on the sprayed scaffold boosts the PCE of small-area cells up to 17.5% that corresponds to an increase of more than 15% compared to standard cells. For large-area (1.1 cm^2) cells, a PCE up to 14.96% is achieved. Moreover, graphene-doped $mTiO_2$ layer enhances the stability of the PSCs compared to standard devices. The feasibility of PSC fabrication by spray coating deposition of the mesoporous film on large-area 21 $\times$ 24 cm^2 provides a viable and low-cost route to scale up the manufacturing of low-cost, stable and high-efficiency PSCs.

Introduction

The power conversion efficiency (PCE) of solution-processed solar cells underwent a rapid progress, especially in the case of the organic–inorganic hybrid perovskite solar cells (PSCs), showing a record high PCE value of 22.7% in 2017 [1]. A prototypical PSC architecture comprises an organometal halide perovskite-based light-harvesting layer, sandwiched between a hole-transporting layer (HTL) and an electron-transporting layer (ETL) [2, 3]. In particular, for the so-called mesoscopic structure, a mesoporous TiO_2 ($mTiO_2$) ETL is usually deposited onto a compact TiO_2 ($cTiO_2$) hole-blocking layer as photoelectrode (PE) scaffold. The $mTiO_2$ layer has a dual role consisting in both extracting the photo-generated electrons from the perovskite layer and transporting the charge towards the transparent conductive oxide (TCO) [2, 3]. The mesoporous scaffold structure accelerates the charge separation and the electron injection from the perovskite to the ETL [4], which allows the most efficient [5] and stable [6] PSCs to be fabricated. The photovoltaic performance achieved by PSCs with mesoscopic TiO_2 architectures (PCE >

20%) [7, 8] is encouraging the scientific community to scale up this technology. The possibility to fabricate large-area mesoscopic PSCs has already been proved in our recent work on graphene-based modules by adopting spin coating-based manufacturing. However, in this case, the module size is limited by the spin coater dimensions, which restricts the module active area to a few tens of cm^2 [9, 10]. Alternative deposition techniques, such as screen printing [11], blade coating [12], spray coating [13] and electrospray coating [14, 15], have been considered with efficiency on small-area cells of 9.3%, 9.7%, 16% and 15%, respectively. However, their applicability to large-area format compatibly with the controlled deposition of uniform $mTiO_2$ films is still an open issue [15].

Differently from a wet film deposition (typical of spin and blade coating, as well as screen printing techniques), during spray coating of $mTiO_2$ films, small droplets of material are deposited onto the substrate [16]. Consequently, spray coating is not affected by the roughness of the underlying layer or by the substrate pattern [17] and it can be applied on irregular surfaces with high reproducibility [18]. Moreover, the spray coating technique allows the whole device area to be covered in a second timespan without any restriction in term of dimensions and geometry. Lastly, the possibility to spray any dispersion independently by the mixed precursors or doping materials makes the spray coating advisable to speed up and scale up the perovskite modules fabrication [13, 19] for their market entry [20–22]. Based on these considerations, Huang *et al* [13] demonstrated superior charge transport properties for sprayed $mTiO_2$ nanoparticles compared to the corresponding spin-coated film, allowing PSCs to reach PCE exceeding 16%. Moreover, PCE above 15% has been recently demonstrated for small-area PSCs based on electrospray-coated $mTiO_2$ as photoelectrode (PE) scaffold [15]. Despite these advances, the application of spray coating techniques to large-area PSCs is still limited to few cases [23–25], and the all-sprayed devices achieved PCEs which are still far ($\leqslant$11.7%) from the state-of-the-art [1]. Recently, both PCE and the stability of PSCs have been improved by exploiting 2D materials, e.g. graphene or MoS_2, to control the interface properties between the different layers in the PSC architecture [9, 10]. The advantage of this strategy, named as 'Graphene Interface Engineering' (GIE), is linked with the possibility to create and design layered artificial structures with on-demand electrochemical properties [26–30] by means of scalable, cost-effective and solution-processed methods [31–36]. In fact, the possibility to produce 2D materials from the exfoliation of their bulk counterparts in suitable liquids [37–43] enables the formulation of functional inks [44–47]. Subsequently, 2D material inks can be deposited onto different substrates by well-established printing/coating techniques [48–53].

Based on the aforementioned considerations, graphene-based hole-blocking layer (or ETL) have demonstrated to reduce the energy barriers for electron collection at the PE, improving the short-circuit current density (J_{SC}) [54–56]. For example, graphene/metal oxide composites improved the J_{SC} of 23% compared to the one of graphene-free counterpart [54]. Graphene quantum dots (GQDs) and a lithium neutralized graphene oxide (GO-Li) have been used as interlayers between the $mTiO_2$ and the perovskite absorber in a mesoscopic PSCs [55, 56] to accelerate the electron injection. Consequently, GQDs-based PSCs exhibited faster electron extraction time (90–106 ps) compared to the PSCs without GQD (260–307 ps), while the use of GO-Li improved the linear trend of $J_{SC} - P_{inc}$ curves with respect to that expressed by the reference cells. Additionally, graphene has also been used to dope the $mTiO_2$ [57, 58]. Actually, the presence of graphene into $mTiO_2$-based ETLs reduced the interfacial resistance and improved the electron collection efficiency at the PE as demonstrated by a two-fold faster electron diffusion coefficient than the native ETL [57]. In particular, PSC based on graphene-doped $mTiO_2$ (Gr–$mTiO_2$) layer deposited by spin coating has shown a record PCE above 16% and also improved stability, retaining more than 88% of the initial performance over 16 h of prolonged 1 SUN illumination at maximum power point (MPP) [58]. Actually, it is well-established that GIE is also an effective tool for the fabrication of efficient and durable PSCs [59].

Herein, we report the use of the GIE in order to fabricate PSCs via automated spray coating (ASC) technique. The ASC enables Gr–$mTiO_2$ to be deposited compatibly with high-throughput serial manufacturing of PSCs. The optimization of sprayed $mTiO_2$ is assessed by studying its morphological, structural and electronic properties as a function of the substrate temperature and the concentration of $mTiO_2$ paste. The sprayed Gr–$mTiO_2$ paste allows PSCs to reach a PCE of 17.5% and 14.96% on 0.1 cm^2 and 1.1 cm^2 active areas, respectively. The use of graphene enables the PSC efficiency to be improved more than 16% compared to the reference device. Finally, electro-optical analysis points out the beneficial role of graphene in the electron injection, trap states and charge transport into the PE. Lastly, we show that the use of graphene into the $mTiO_2$ partially mitigates the degradation phenomenon at the perovskite/ETL interface, thus increasing the PSCs time life under operative conditions.

Methods

Graphene ink preparation

Liquid phase exfoliation of graphite flakes [60] (Sigma-Aldrich) in N-methyl-2-pyrrolidone (NMP) and subsequent solvent exchange process [61] were used to prepared graphene flakes ink in ethanol (EtOH, Sigma-Aldrich, +99.8%) at a concentration of

0.9 mg ml^{-1}. Experimentally, 3 g of graphite flakes were dispersed in 300 ml of NMP and ultrasonicated for 6 h. The obtained dispersion was then ultra-centrifuged at 16 000 g (in a Beckman Coulter Optima™ XE-90 with a SW32Ti rotor) for 30 min at 15 °C, exploiting sedimentation-based separation to remove thick flakes and un-exfoliated graphite. After the ultracentrifugation process, 80% of the supernatant was collected by pipetting. The pipetted sample was dried using a rotary evaporator at 70 °C, 5 mbar, then 500 ml of EtOH were added to the dried sample. The sample was then dispersed using a sonic bath for 10 min. Subsequently, the sample was centrifuged at 800 g (in a Beckman Coulter Optima™ XE-90 with a SW32Ti rotor). Then, the sediment was collected while the supernatant was discarded. This process of decantation was repeated twice, with the objective to wash out the NMP residuals. Finally, the sediment was dispersed in 200 ml of EtOH.

Solar cells fabrication

The solar cells were fabricated on Glass/FTO substrates, which were previously and consecutively washed for 10 min with acetone, deionized water and EtOH, in an ultrasonic bath. A TiO_2 dispersion, for spray pyrolysis deposition of $cTiO_2$, consisted of 0.16 M diisopropoxytitaniumbis acetylacetonate (TiAcAc) and 0.4 M acetylacetone (AcAc) in EtOH. The final thickness of the $cTiO_2$, deposited at a temperature of 450 °C onto the pre-cleaned laser patterned FTO glass, was 50 nm. For $mTiO_2$ film deposition, anatase TiO_2 nanoparticles paste (18NR-T, Dyesol) was used. The $mTiO_2$ paste was dissolved into EtOH via stirring and ultrasonic bath to obtain 1.4 M, 1.6 M, 1.7 M and 1.8 M concentrations. Mesoscopic TiO_2 films based on the aforementioned concentrations were deposited by ASC technique. Then, 0.4 M of TiAcAc was added to the $mTiO_2$ dispersion, which was stirred for 1 h. Subsequently, the obtained dispersion was doped with graphene flakes dispersion in EtOH (concentration of 0.5%, 1% and 2% v/v were tested). The $mTiO_2$ was finally deposited onto the FTO/compact TiO_2 substrates by means of ASC using setting deposition parameters reported in table S1. For reference spin-coated $mTiO_2$-based devices, TiO_2 paste (18NR-T, Dyesol) was diluted with EtOH, (w/w ratio of 1:5), and spin-coated onto the $cTiO_2$ surface at 1500 rpm for 20 s. The formed $mTiO_2$ films were sintered at 480 °C for 30 min using a previously reported protocol [62]. The $CH_3NH_3PbI_3$ absorber layer was deposited by a crystal engineering method in atmospheric condition [62]. Briefly, 535 mg of PbI_2 powder was dissolved in 1 ml DMF and spin-coated at 6000 rpm for 10 s, while the temperature of the dispersion was set to 70 °C, on the surface of the preheated (70 °C) $mTiO_2$ film. Subsequently, the devices were annealed at 40 °C for 2 min (temperature raise time = 1 min)) and at 60 °C for 1 min (temeperature raise time = 1 min). In the second step, the cooled PbI_2 layers were dipped in a solution of methylammonium iodide (CH_3NH_3I in anhydrous 2-propanol 10 mg ml^{-1}) for 10 min at room temperature while the solution was kept under mechanical stirring during the dipping time. Then, the devices were washed immediately by spin coating 2-propanol with an acceleration rate of 6000 rpm for 10 s. Finally, the devices were heated at 70 °C for 2 min (temperature raise time = 1 min), and at 115 °C for 4 min (temperature raise time = 3 min) with relative humidity of about 40% on a hotplate. After heat treatment, 100 μl of spiro-OMeTAD (73.5 mg ml^{-1}) in chlorobenzene (CB) solution, doped with 26 μl of tert-butylpyridine (TBP), 16.6 μl of Lithium Bis (Trifluoromethanesulfonyl) Imide (Li-TFSI) of stock solution (520 mg in 1 ml acetonitrile), and 7.2 μl of cobalt (III) complex solution (FK209 from Lumtec), was deposited as HTL by spin coating at 2000 rpm for 20 s. Finally, 80 nm of Au was deposited as counter electrode by thermal evaporation.

Characterization

Masked devices were tested by acquiring *I–V* curves under a Class A solar simulator (ABET Sun 2000) at AM1.5 and 100 mW/cm^2 illumination conditions calibrated with a reference silicon cell (RERA Solutions RR-1002), using a Keithley 2420 as a source-meter in ambient condition without sealing. Sun simulator spectrum and class were measured with a BLACK-Comet UV–VIS Spectrometer.

The atomic force microscopy (AFM) analysis of the surface of the TiO_2 thin films, realized by spray or spin coating, was performed through an A.P.E. Research Atomic Force Microscope. Measurements were performed in non-contact mode with a silicon tip with a radius of 8 nm, mounted on a cantilever (resonance frequency = 325 kHz) with a spring constant of 40 N m^{-1}.

Dark *I–V*, transient photovoltage (TPV), stability stress test at the MPP, and illumination intensity dependence of the V_{oc} and J_{sc} were performed with a high speed four channel source meter. A white LED array (4200 Kelvin) tuneable up to 200 mW/cm^2 of optical power density-based measurement system (Arkeo-Cicci research s.r.l.) was used as light source. A spring contact-based sample holder was used to improve the repeatability of the experiments.

Incident power conversion efficiency (IPCE) spectra were aquired by using a homemade setup.

Electrochemical measurements were performed in dark conditions at room temperature using an Autolab 302N Modular Potentiostat from Met Rohm in the two-electrode configuration with a bias voltage ranging from 0.6 to 1 V. The sinewave perturbation used was 10 mV of amplitude with frequencies from 1 MHz to 1 Hz.

The surface morphology of mesoporous layers and cross section image were obtained by using scanning electron microscope (SEM) FE-SEM ZEISS.

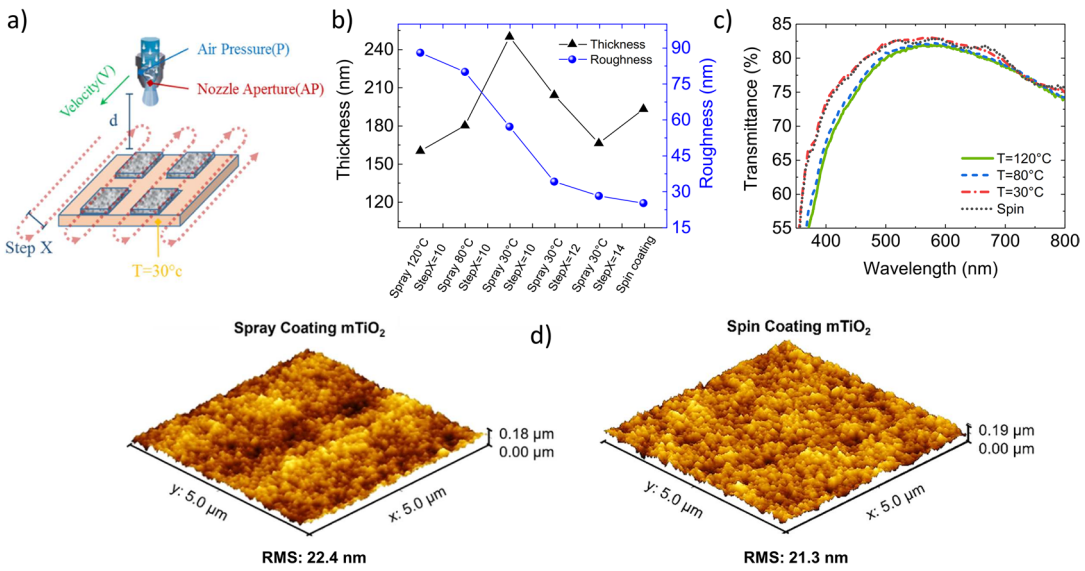

Figure 1. (a) Scheme of the automated spray coating. (b) Thickness and roughness of TiO_2 films, by spray coating deposition at 30 °C, 80 °C, 120 °C and by spin coating. (c) Transmittances of TiO_2 film spray-coated on different temperatures of the substrate. (d) AFM topography of the different $mTiO_2$ thin films prepared by ASC at 30 °C (left) and by spin coating (right).

Results and discussion

In mesoscopic PSCs, the light enters from the PE to excite the photoactive layer. Therefore, the light passes through the $mTiO_2$ layer before reaching the perovskite overlayer. For this reason, the control of optical transparency, thickness and roughness of the TiO_2 film are crucial to achieve efficient PSCs [63, 64].

The morphological and optoelectronic properties of the final sprayed $mTiO_2$ layer depend by several deposition parameters, i.e. the substrate temperature, the number of spray cycles, the distance between the spray nozzle and the substrate, the nozzle aperture, the air pressure, and, lastly, the distance between two adjacent spray lines (StepX) [65, 66] (see figure 1(a)).

As a first step in the deposition optimization of the ASC process, we studied the influence of the substrate (i.e., FTO) temperature on the roughness and transparency of the resultant $mTiO_2$ layer. Spin coating deposition of $mTiO_2$ was also considered for comparison. Spray coating of commercial $mTiO_2$ nanoparticles (18NRT) dispersed in EtOH (1:5 w/w ratio) was accomplished on the substrate heated at different temperatures (30, 80 and 120 °C). As shown in figures 1(b) and (c), the highest substrate temperature (120 °C) resulted in a rough $mTiO_2$ surface (>80 nm), which caused a decrease of the average electrode transmittance (81.4%) compared to that obtained with the other temperature depositions (83% for $mTiO_2$ obtained by spray at 30 °C and spin coating). On the other hand, the low substrate temperatures (30 and 80 °C) allowed the solvent to reach the substrate surface with a consequent flattening of the $mTiO_2$ surface. Notably, the RMS roughness of the layer was also influenced by the overlap of two adjacent spray lines. The $mTiO_2$ film deposited by using a distance between two adjacent spray lines of 14 mm (StepX = 14 mm) had the best width overlay of each sprayed spot (5 mm), since it results in lower roughness (28 nm) than those obtained by adopting other StepX values. Atomic force microscopy topographies (figure 1(d)) show that the sample realized by ASC has a root means square (RMS) roughness (22.4 nm) comparable to that of the spin-coated samples (21.3 nm) (see also table S2).

The $mTiO_2$ film morphology obtained for the deposition at 30 °C enabled the PSCs performance to be enhanced compared to that of the PSCs produced with higher temperatures, i.e. 80, 100 and 120 °C (figure 2(a)). More in detail, the PCE decreased by almost 60% and 80% when the substrate temperature for the $mTiO_2$ spray coating increased from 30 to 80 °C and 120 °C, respectively. However, it is noteworthy that the highest PCE obtained for sprayed $mTiO_2$-based PSCs (13.92%) was still 34% lower than that of reference PSCs produced by spin coating $mTiO_2$ (15.69%).

In order to optimize the sprayed $mTiO_2$ layer morphology, different concentrations of TiO_2 dispersion (1.4 M, 1.6 M, 1.7 M and 1.8 M) were used and titanium diisopropoxide bis acetylacetonate (TiAcAc) was added to the sprayed dispersion to improve the connectivity between the $mTiO_2$ nanoparticles [13] (details about the analysed concentrations are reported in the methods section). By adjusting spray parameter settings, (table S1), the $mTiO_2$ film with thicknesses ranging from 150 to 200 nm [5, 67, 68] exhibited the lowest RMS roughness values (about 22 nm) (figure S1) (stacks.iop.org/TDM/5/045034/mmedia). Therefore, small-area (0.1 cm^2) PSCs were produced with a $mTiO_2$ film thicknesses of 180 nm, as shown by a representative cross-sectional SEM image (figure S2). The as-prepared cells without TiAcAc resulted in maximum PCE of 9.1%. The addition of TiAcAc into

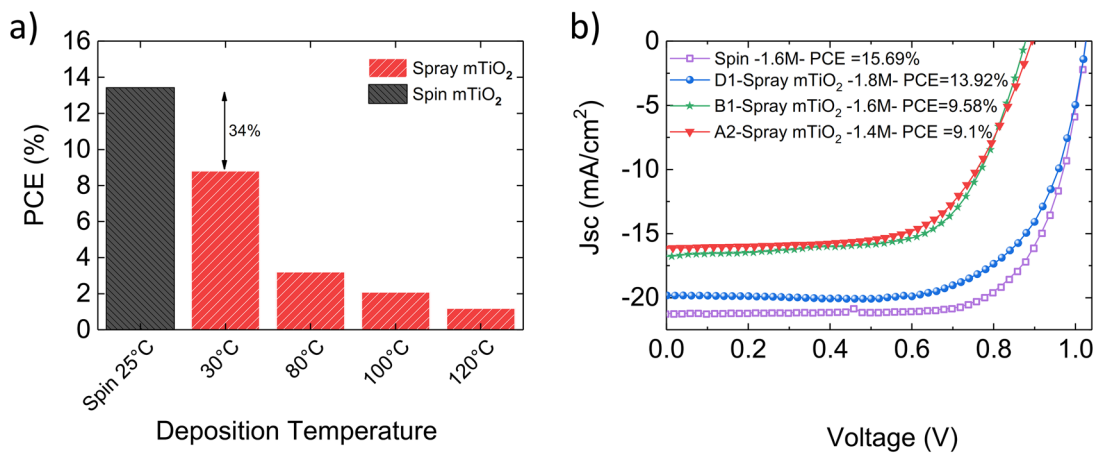

Figure 2. (a) PCE under 1 SUN illumination for sprayed-$mTiO_2$-based PSCs, realized by varying the substrate deposition temperature. (b) Density of current–voltage (I–V) curves under 1 sun for complete PSCs realized by using three different $mTiO_2$ dispersion concentrations with optimum deposition setting.

Table 1. PSCs V_{oc}, J_{sc}, FF and PCE values for three different $mTiO_2$ dispersion concentrations with about 180 nm of sprayed $mTiO_2$ thickness, compared with those of standard spin-coated $mTiO_2$-based cells. Depositions have been performed with 30 °C of substrate temperature and with StepX of 14 mm.

Cell type	V_{oc} (V)	J_{sc} (mA cm^{-2})	FF (%)	PCE (%)	J_{sc} from integrated IPCE (mA cm^{-2})
A2 spray coating 1.4 M (nozzle AP = 8, P = 1.5 bar)	0.871	−15.88	66.34	9.18	−14.95
Spray coating 1.6 M without TiAcAc (nozzle AP = 9, P = 1.5 bar)	0.857	−15.41	65.80	8.69	−14.67
B1 spray coating 1.6 M (nozzle AP = 9, P = 1.5 bar)	0.873	−16.60	66.10	9.58	−16.09
D1 spray coating 1.8 M (nozzle AP = 9, P = 1 bar)	1.021	−19.77	68.94	13.92	−19.40
Standard spin coating	1.018	−21.16	72.82	15.69	−20.65

$mTiO_2$ dispersion resulted in a cell PCE improvement of +10% (table 1). Notably, the highest average PCE of 13.92% was achieved for the PSCs produced by using a $mTiO_2$ concentration of 1.8 M. As shown in figure 2(b), the PCE enhancement was a consequence of the higher current density (J_{sc}) (−19.77 mA cm^{-2}) and Fill Factor (FF) (69%) compared with those of the PSCs fabricated with other $mTiO_2$ dispersion concentrations (1.4 M, 1.6 M and 1.7 M). These effects can be ascribed to an effective crystallization of the perovskite into the 22 nm-rough $mTiO_2$, which help to reduce carrier recombination and improve carrier transport and collection properties [69–71].

The pore size for efficient infiltration of the perovskite into the $mTiO_2$ (figure S3) leads to the highest electron mobility and the lowest disorder in the interface with perovskite.

Although the sprayed $mTiO_2$-based PSCs achieved PCE of ~14%, their J_{sc} and FF were still 10% lower than those of spin-coated $mTiO_2$-based PSCs (table 1), suggesting that the electron recombination at $mTiO_2$/perovskite interface significantly affected the cell performance for sprayed $mTiO_2$-based devices compared to that of spin-coated $mTiO_2$-based ones [72, 73].

With the aim to boost further the performance of the PSCs obtained by ASC, the $mTiO_2$ dispersion was enriched with graphene flakes, resulting in hybrid mesoscopic films, herein named Gr–$mTiO_2$. Graphene flakes were produced by the LPE [44] in NMP. The synthetic procedure is detailed in reference [58] and summarized in the experimental section. Three different concentrations of graphene flakes dispersion (0.5%, 1% and 2% v/v) were tested by fabricating PSCs with active active area of 0.1 cm^2. In agreement with the SEM images of the $mTiO_2$ surface morphology (figure S3), the Gr–$mTiO_2$ films did not show any difference compared to the pristine $mTiO_2$ films. Moreover, the films deposited by spray and spin coating have shown the same surface morphology with an average $mTiO_2$ particle size of ~21 nm.

In term of photovoltaic performance of the PSCs, the optimum concentration of graphene inside $mTiO_2$ was 1% v/v, which results in an increase of J_{sc} and PCE of 13% and 23%, respectively, compared to those of the graphene-free reference (figure S4). This means that a concentration of 1% v/v of graphene dispersion concentration into $mTiO_2$ dispersion can suppress the electron recombination, increasing the J_{sc}. However, once graphene concentration exceeded 1% v/v, the PSC performance decreased. This trend can be ascribed to the increase of Gr–$mTiO_2$ light absorption by increasing graphene flakes concentration that strongly affects the optical transmittance of the PE (see figure S5) [74]. This effect was also observed in the per-

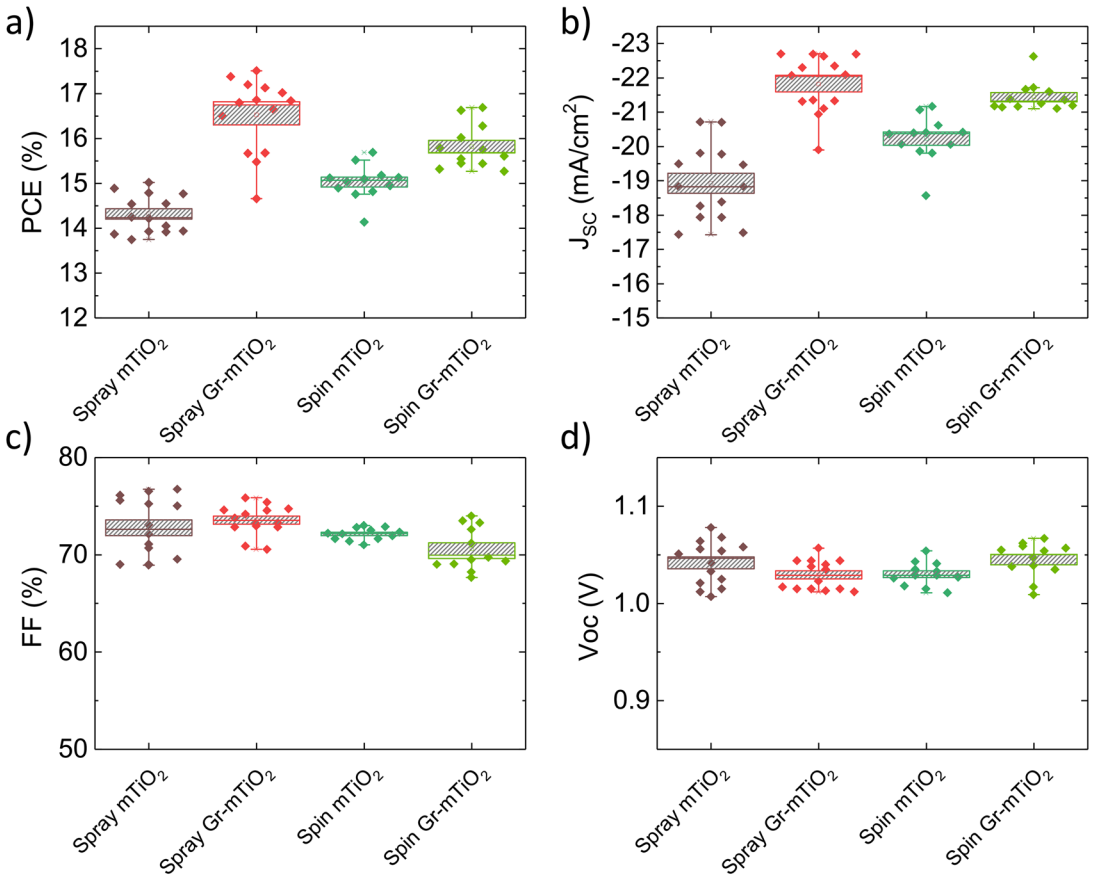

Figure 3. Comparison of electrical parameter statistics for 26 small-area (0.1 cm^2) PSCs based on pristine mTiO$_2$ and 26 small-area PSCs based on Gr–mTiO$_2$ scaffold deposited by ASC and spin coating techniques. The cells were measured under 1 SUN AM 1.5G illumination.

formance of graphene-based cells, in which J_{sc} begins to decrease beyond the optimum graphene loading of 1% v/v (see figure S4(a)).

Perovskite solar cells with and without graphene and for both spray and spin coating of mTiO$_2$ were fabricated and compared. To deposit mTiO$_2$ by ASC, the optimized graphene dispersion with a concentration of 1% v/v was incorporated into the 1.8 M mTiO$_2$ dispersion. In order to demonstrate the uniformity of large-area mTiO$_2$ obtained by ASC, spray coating was firstly accomplished on a large-area substrate (24 × 20 cm^2). Secondly, the substrate was divided into 2.5 × 2.5 cm^2 pieces, subsequently selected from different areas of the initial substrate, to finalize the fabrication of the entire PSCs. On these substrates, devices were made with different active areas 0.1 cm^2 and 1.1 cm^2 (herein named small- and large-area PSCs, respectively) by using the deposition parameter settings, which were previously optimized (see Methods section for details).

Figure 3 reports the electrical parameters (PCE, J_{sc}, FF and V_{OC}) for PSCs based on pristine mTiO$_2$ and Gr–mTiO$_2$ deposited by ASC and spin coating techniques. Notably, for both deposition techniques, the PSCS based on Gr–mTiO$_2$ led to a significant enhancement of J_{sc} with respect to the ones with pristine mTiO$_2$. In particular, for small-area cells (0.1 cm^2), the PSCs based on spray-deposited Gr–mTiO$_2$ led to a ~16% increase of J_{sc} compared to the mTiO$_2$-based ones, whereas the graphene doping for spin-coated mTiO$_2$ improved the J_{sc} of 5% with respect to the graphene-free reference PSC.

The average PCE of spray Gr–mTiO$_2$ based devices was 16.8%, i.e. higher than the spin-coated mTiO$_2$-based PSCs (15.6%). For pristine sprayed mTiO$_2$-based PSC, the average J_{SC}, FF and V_{OC} values were 18.7 mA cm^{-2}, 0.72 and 1050 mV, respectively. By introducing graphene flakes into the mTiO$_2$, average J_{sc} increased up to 22.2 mA cm^{-2}, while V_{oc} and FF values did not undergo significant variations. Therefore, our champion cell exhibited 17.5% PCE, exceeding the highest PCE previously reported for a two-step process (0.1 cm^2 active area) $CH_3NH_3PbI_3$-based PSC using spin-coated mTiO$_2$ layer (PCE 17%) [62, 75].

The characterization of large-area (1.1 cm^2) cells (see table 2 and figure S6) confirmed the J_{sc} enhancement for Gr–mTiO$_2$-based cells compared to that of pristine mTiO$_2$-based reference (from −18.5 to −20.1 mA cm^{-2}).

Time-dependent PCE response (figure S7(a)) and *I*–*V* curves as a function of the scan voltage direction (figure S7(b)) did not evidence the presence of hysteresis [8].

Table 2. Electrical parameters of sprayed large area (1.1 cm^2) PSCs with and without graphene into $mTiO_2$ in comparison to those of PSCs using spin-coated $mTiO_2$. All the devices were measured under 1 sun AM 1.5G illumination.

Type of cells	V_{oc} (V)	J_{sc} (mA cm^{-2})	FF (%)	PCE (%)
Spray pristine $mTiO_2$	1.063	−18.571	66.712	13.165
	(1.05 ± 0.012)	(−18.91 ± 0.46)	(65.15 ± 2.14)	(12.94 ± 0.26)
Spray Gr–$mTiO_2$	1.059	−20.199	69.957	14.963
	(1.06 ± 0.005)	(−19.79 ± 0.43)	(67.25 ± 2.54)	(14.21 ± 0.80)
Spin $mTiO_2$	1.031	−17.039	65.488	11.503
	(1.04 ± 0.008)	(−18.12 ± 0.96)	(62.6 ± 2.50)	(11.78 ± 0.29)
Spin Gr–$mTiO_2$	1.03	−19.224	68.199	13.506
	(1.04 ± 0.01)	(−19.02 ± 0.19)	(65.22 ± 4.11)	(12.91 ± 0.91)

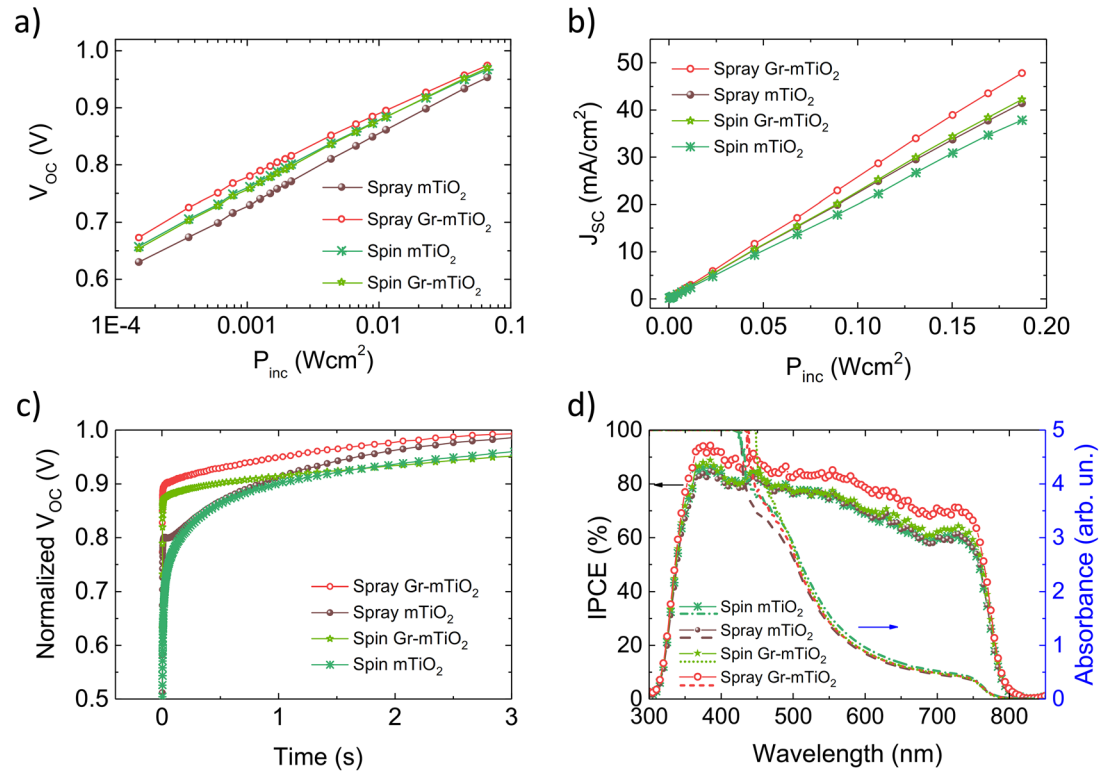

Figure 4. (a) V_{OC} versus P_{inc}, (b) J_{SC} versus P_{inc} and (c) V_{OC} rise profiles normalized at the maximum value, (d) absorption and IPCE spectra for the tested PSCs.

The role of graphene in to the $mTiO_2$ film: electro-optical analysis

In order to fully understand the differences between the pristine $mTiO_2$ and the Gr–$mTiO_2$ based devices, complementary electrical measurements (V_{oc}/J_{sc} versus light intensity) were performed for each device typology.

The relation between V_{oc} and the incident light power (P_{inc}) (figure 4(a)) allowed the recombination processes at the $mTiO_2$/perovskite interface to be evaluated [76, 77]. V_{OC} versus P_{inc} trends recorded for all the tested device typologies have shown a logarithmic increase with similar slope values (124 mV dec^{-1} for spray reference-$mTiO_2$, 119 mV dec^{-1} for spray Gr–$mTiO_2$ and 122 mV dec^{-1} for spin $mTiO_2$ and spin Gr–$mTiO_2$). This means that Gr–$mTiO_2$ based ETL did not significantly influence charge recombination rate over a wide operating light intensity window (from 0.1 to 100 mW cm^{-2}). The higher V_{oc} absolute values recorded for Gr–$mTiO_2$ based device compared to that of graphene-free devices was correlated with the reduced interfacial charge recombination at TiO_2/perovskite, in agreement with previous reports [78].

The variation of J_{sc} versus P_{inc} is reported in figure 4(b). Since the $J_{sc} - P_{inc}$ slope increased with the efficiency of charge collection at the device contacts [79], it can be concluded that sprayed Gr–$mTiO_2$ layer with 266 mA W^{-1} slope effectively collected the photogenerated electrons from the perovskite absorber. Finally, transient V_{oc} rise measurements, reported in figure 4(c), were carried out by suddenly switching on the 1 SUN illumination from the dark steady state condition ($t = 0$ s) and monitoring the subsequent rise in photovoltage. The time rise of V_{oc} for PSC with Gr–$mTiO_2$ was shorter than the reference device. This indicated that an efficient active layer regeneration and/or charge-trans-

Table 3. The resistivity and conductivity of pristine $mTiO_2$ and the Gr–$mTiO_2$, measured through four-point probe.

Mesoporous scaffold sintered at 450 °C	Resistivity ρ (Ω cm)	Conductivity σ (Siemens cm)
Spray $mTiO_2$	3.6×10^5	2.7×10^{-6}
Spray Gr–$mTiO_2$	2.4×10^5	4.2×10^{-6}

fer process between the active and the transport layers occurred in presence of graphene flakes [80]. The fast rises for PSC with Gr–$mTiO_2$ can be ascribed to a fast filling and stabilization of charge trap states by injected or photogenerated electrons, reducing the availability of trap sites to mediate non-radiative recombination [81]. The rise time of V_{oc} obtained for our PSCs evidenced an electron injection improvement at perovskite/$mTiO_2$ interface when $mTiO_2$ was doped with graphene [82].

According to the electrical parameter statistic graphs (figure 3), a dual effect of the Gr–$mTiO_2$ on device performance is evidenced. First, the presence of graphene in the $mTiO_2$ scaffold can deform the perovskite grain due to ferroelectric distortion at graphene/perovskite interfaces which affects the perovskite crystallization process [78, 82]. This can cause an efficient electron injection at the Gr–$mTiO_2$/perovskite interface [58]. Second, graphene can assist the negative carrier transport within the TiO_2 layer by increasing electron mobility, which results in increasing the PSCs photocurrent density [83].

In order to further investigate the enhancement of the device performance through the incorporation of graphene into the $mTiO_2$, the effects of the absorber layer and conductivity of TiO_2 layer were characterized. A four-point probe system was used to measure the resistivity of pristine and Gr–$mTiO_2$. As reported in table 3, Gr–TiO_2 has shown a 55% increase of the conductivity with respect to that of pristine $mTiO_2$.

Furthermore, sprayed Gr–$mTiO_2$-based PSCs have shown an improvement in the photocurrent density, which is defined by integrating IPCE over the absorption wavelength range. Actually, IPCE(λ) is the product of three factors: light harvesting efficiency (η_{LH}) depending on the perovskite layer, the quantum yield of charge injection from exited perovskite to ETL and HTL (η_{INJ}) and the charge carrier collection efficiency (η_{COL}) at the electrodes (IPCE $= \eta_{LH}\eta_{INJ}\eta_{COL}$) [84]. In addition, the η_{INJ} is defined as the product between the electron injection (η_{EINJ}) and hole injection (η_{HINJ}) efficiency, as well as collection efficiency is defined as the product between the electron collection (η_{ECOL}) and hole collection efficiencies η_{HCOL} respectively:

$$\eta_{INJ} = \eta_{EINJ}\eta_{HINJ}$$

$$\eta_{COL} = \eta_{ECOL}\eta_{HCOL}.$$

Figure 4(d) shows the absorption spectra of perovskite grown on both $mTiO_2$ and Gr–$mTiO_2$ scaffolds, evidencing that they are perfectly overlapped. This means that the modified Gr–TiO_2 layer did not affect the perovskite light harvesting properties. Consequently, since the two structures differed only in the addition of graphene within the ETL, the η_{LH}, η_{HINJ} and η_{HCOL} can be considered equal for both structures. Therefore, enhancement of IPCE in graphene-based devices can be likely ascribable to higher η_{EINJ} at the perovskite/HTL interface and improved η_{ECOL} at the PE compared to those of reference device. Such analysis agrees with the V_{OC} rise and V_{OC}/J_{SC} versus P_{inc} trends previously discussed.

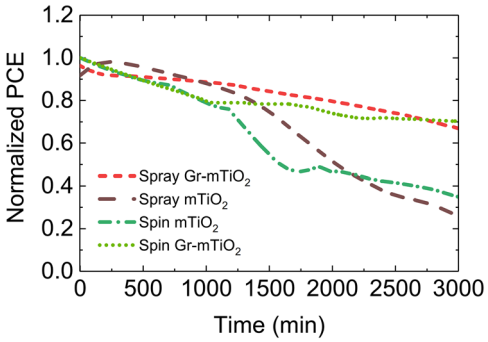

Figure 5. PCE aging trends under prolonged 1 SUN white LED illumination at MPP for the tested device typologies.

Stability test

One of the most crucial challenges for mesoscopic PSCs is the stability under real working condition [85]. Despite numerous efforts by the scientific community to develop more stable PSCs, many issues are still opened since perovskite degradation strongly depends on light, moisture, and temperature [86–88].

Based on these considerations, we compared the stability of encapsulated PSCs based on pristine sprayed $mTiO_2$ and Gr–$mTiO_2$, respectively, by continuously exposing them under 1 SUN illumination for 2 d at 50 °C and 55% relative humidity of ambient air. The *I–V* characteristics were progressively acquired during the ageing time at MPP. The extracted electrical parameters are reported in figure 5, normalized to the value obtained at $t = 0$ min. Notably, the cells based on sprayed Gr–$mTiO_2$ have shown a remarkable stability by retaining more than 80% of the initial PCE value after more than 40 h of the stress test, whereas the PCE of the spray pristine $mTiO_2$ cells decayed by 50% over the first 25 h of operation.

As discussed in the previous section, the Gr–$mTiO_2$ has an electrical conductivity able to optimize charge collection [89–92] and separation [80, 91] at the PE. The charge extraction properties at the PE drastically reduces the trapped charges accumulated at the $mTiO_2$/perovskite interface. This can slow down the perovskite degradation [93]. Moreover, as discussed by Busby *et al* [94] through ToF-SIMS measurements, the presence of graphene into the $mTiO_2$ limits the Ti–I bonding preserving a compact $CH_3NH_3PbI_3$ layer

upon the light-induced ageing. We should also point out that 2D materials can improve thermal stability by reducing surface degradation of perovskite [95].

Conclusion

The field of perovskite solar cells (PSCs) is rapidly moving toward consolidating deposition processes that can be extended to large-area for industrial exploitations. In this work, we reported that the combined use of automatized spray coating techniques and graphene doping of $mTiO_2$ is an effective strategy to improve photovoltaic performances of PSCs with respect to the conventional, lab-scale device produced by spin coating process. More in detail, the PSC fabricated on a small-area with spray-coated Gr–$mTiO_2$ has shown an average power conversion efficiency (PCE) of 16.8% (max 17.5%), which is remarkably superior to that obtained for PSC using graphene-free sprayed (14.3%) or spin-coated $mTiO_2$ (15.1%). These results were also confirmed on large-area cells, which achieved a PCE of 14.96% using spray-coated Gr–$mTiO_2$, against 13.1% obtained by the reference PSCs. Electro-optical characterizations and transient measurements have shown that graphene doping of TiO_2 can improve the electron transport in ETL and charge injection at perovskite/ETL interface. In addition, Gr–$mTiO_2$ layer strongly affected the stability of PSCs under prolonged (47 h) light soaking conditions by enlarging the lifetime of the devices, which retained more than 80% of the initial PCE value. These results pave the way to realize stabilized mesoscopic perovskite solar modules with a versatile, low-cost and roll-to-roll compatible printing technique.

Acknowledgments

This project has received funding from the European Union's Horizon 2020 research and innovation programme under grant agreement No. 785219—GrapheneCore2. A D C gratefully acknowledge the financial support of the Ministry of Education and Science of the Russian Federation in the framework of Increase Competitiveness Program of NUST 'MISiS' (No. K2-2017-025), implemented by a governmental decree dated 16th of March 2013, N 211.

ORCID iDs

Antonio Agresti https://orcid.org/0000-0001-6581-0387
Francesco Bonaccorso https://orcid.org/0000-0001-7238-9420
Aldo Di Carlo https://orcid.org/0000-0001-6828-2380

References

[1] www.nrel.gov/pv/assets/pdfs/pv-efficiencies-07-17-2018.pdf
[2] Mei A *et al* 2014 A hole-conductor-free, fully printable mesoscopic perovskite solar cell with high stability *Science* **345** 295
[3] Nah Y-C, Paramasivam I and Schmuki P 2010 Doped TiO_2 and TiO_2 nanotubes: synthesis and applications *ChemPhysChem* **11** 2698–713
[4] Ponseca C S *et al* 2014 Organometal halide perovskite solar cell materials rationalized: ultrafast charge generation, high and microsecond-long balanced mobilities, and slow recombination *J. Am. Chem. Soc.* **136** 5189–92
[5] Yang W S *et al* 2017 Iodide management in formamidinium-lead-halide—based perovskite layers for efficient solar cells *Science* **356** 1376
[6] Grancini G *et al* 2017 One-year stable perovskite solar cells by 2D/3D interface engineering *Nat. Commun.* **8** 15684
[7] Yang J, Fransishyn K M and Kelly T L 2016 Comparing the effect of mesoporous and planar metal oxides on the stability of methylammonium lead iodide thin films *Chem. Mater.* **28** 7344–52
[8] Kim H-S and Park N-G 2014 Parameters affecting *I–V* hysteresis of $CH_3NH_3PbI_3$ perovskite solar cells: effects of perovskite crystal size and mesoporous TiO_2 layer *J. Phys. Chem. Lett.* **5** 2927–34
[9] Agresti A *et al* 2017 Graphene interface engineering for perovskite solar modules: 12.6% power conversion efficiency over 50 cm^2 active area *ACS Energy Lett.* **2** 279–87
[10] Matteocci F *et al* 2016 High efficiency photovoltaic module based on mesoscopic organometal halide perovskite *Prog. Photovolt.* **24** 436–45
[11] Matteocci F, Razza S, Di Giacomo F, Casaluci S, Mincuzzi G, Brown T M, D'Epifanio A, Licoccia S and Di Carlo A 2014 Solid-state solar modules based on mesoscopic organometal halide perovskite: a route towards the up-scaling process *Phys. Chem. Chem. Phys.* **16** 3918–23
[12] Kim H-S *et al* 2012 Lead iodide perovskite sensitized all-solid-state submicron thin film mesoscopic solar cell with efficiency exceeding 9% *Sci. Rep.* **2** 591
[13] Huang H, Shi J, Lv S, Li D, Luo Y and Meng Q 2015 Sprayed P25 scaffolds for high-efficiency mesoscopic perovskite solar cells *Chem. Commun.* **51** 10306–9
[14] Lee H, Hwang D, Jo S M, Kim D, Seo Y and Kim D Y 2012 Low-temperature fabrication of TiO_2 electrodes for flexible dye-sensitized solar cells using an electrospray process *ACS Appl. Mater. Interfaces* **4** 3308–15
[15] Kim M-C, Kim B J, Yoon J, Lee J-W, Suh D, Park N-G, Choi M and Jung H S 2015 Electro-spray deposition of a mesoporous TiO_2 charge collection layer: toward large scale and continuous production of high efficiency perovskite solar cells *Nanoscale* **7** 20725–33
[16] Krebs F C 2009 Fabrication and processing of polymer solar cells: a review of printing and coating techniques *Sol. Energy Mater. Sol. Cells* **93** 394–412
[17] Aziz F and Ismail A F 2015 Spray coating methods for polymer solar cells fabrication: a review *Mater. Sci. Semicond. Process.* **39** 416–25
[18] Nga P P, Joachim N B and Pasqualina M S 2005 Spray coating of photoresist for pattern transfer on high topography surfaces *J. Micromech. Microeng.* **15** 691
[19] Reale A, LaNotte L, Salamandra L, Polino G, Susanna G, Brown T M, Brunetti F and Di Carlo A 2015 Spray coating for polymer solar cells: an up-to-date overview *Energy Technol.* **3** 385–406
[20] Ono L K, Park N-G, Zhu K, Huang W and Qi Y 2017 Perovskite solar cells—towards commercialization *ACS Energy Lett.* **2** 1749–51
[21] Song Z, McElvany C L, Phillips A B, Celik I, Krantz P W, Watthage S C, Liyanage G K, Apul D and Heben M J 2017 A technoeconomic analysis of perovskite solar module manufacturing with low-cost materials and techniques *Energy Environ. Sci.* **10** 1297–305
[22] Berry J J, van de Lagemaat J, Al-Jassim M M, Kurtz S, Yan Y and Zhu K 2017 Perovskite photovoltaics: the path to a printable terawatt-scale technology *ACS Energy Lett.* **2** 2540–4

[23] Bishop J E, Mohamad D K, Wong-Stringer M, Smith A and Lidzey D G 2017 Spray-cast multilayer perovskite solar cells with an active-area of 1.5 cm^2 *Sci. Rep.* **7** 7962
[24] Yang Z, Zhang S, Li L and Chen W 2017 Research progress on large-area perovskite thin films and solar modules *J. Materiomics* **3** 231–44
[25] Das S, Yang B, Gu G, Joshi P C, Ivanov I N, Rouleau C M, Aytug T, Geohegan D B and Xiao K 2015 High-performance flexible perovskite solar cells by using a combination of ultrasonic spray-coating and low thermal budget photonic curing *ACS Photon.* **2** 680–6
[26] Samorì P, Palermo V and Feng X 2016 Chemical approaches to 2D materials *Adv. Mater.* **28** 6027–9
[27] Zhang J, Wang T, Liu P, Liu S, Dong R, Zhuang X, Chen M and Feng X 2016 Engineering water dissociation sites in MoS_2 nanosheets for accelerated electrocatalytic hydrogen production *Energy Environ. Sci.* **9** 2789–93
[28] Xia Z *et al* 2016 Electrochemical functionalization of graphene at the nanoscale with self-assembling diazonium salts *ACS Nano* **10** 7125–34
[29] Najafi L, Bellani S, Oropesa-Nuñez R, Ansaldo A, Prato M, Del Rio Castillo Antonio E and Bonaccorso F 2018 Engineered $MoSe_2$-based heterostructures for efficient electrochemical hydrogen evolution reaction *Adv. Energy Mater.* **414** 1703212
[30] Najafi L, Bellani S, Martín-García B, Oropesa-Nuñez R, Del Rio Castillo A E, Prato M, Moreels I and Bonaccorso F 2017 Solution-processed hybrid graphene flake/2H–MoS_2 quantum dot heterostructures for efficient electrochemical hydrogen evolution *Chem. Mater.* **29** 5782–6
[31] Chen S and Shi G 2017 Two-dimensional materials for halide perovskite-based optoelectronic devices *Adv. Mater.* **29** 1605448
[32] Yang J, Voiry D, Ahn Seong J, Kang D, Kim Ah Y, Chhowalla M and Shin Hyeon S 2013 Two-dimensional hybrid nanosheets of tungsten disulfide and reduced graphene oxide as catalysts for enhanced hydrogen evolution *Angew. Chem., Int. Ed.* **52** 13751–4
[33] Bonaccorso F, Colombo L, Yu G, Stoller M, Tozzini V, Ferrari A C, Ruoff R S and Pellegrini V 2015 Graphene, related two-dimensional crystals, and hybrid systems for energy conversion and storage *Science* **347** 1246501
[34] Bonaccorso F, Lombardo A, Hasan T, Sun Z, Colombo L and Ferrari A C 2012 Production and processing of graphene and 2d crystals *Mater. Today* **15** 564–89
[35] Li S-L, Tsukagoshi K, Orgiu E and Samori P 2016 Charge transport and mobility engineering in two-dimensional transition metal chalcogenide semiconductors *Chem. Soc. Rev.* **45** 118–51
[36] Yang S, Brüller S, Wu Z-S, Liu Z, Parvez K, Dong R, Richard F, Samorì P, Feng X and Müllen K 2015 Organic radical-assisted electrochemical exfoliation for the scalable production of high-quality graphene *J. Am. Chem. Soc.* **137** 13927–32
[37] Nicolosi V, Chhowalla M, Kanatzidis M G, Strano M S and Coleman J N 2013 Liquid exfoliation of layered materials *Science* **340** 1226419–37
[38] Ciesielski A *et al* 2014 Harnessing the liquid-phase exfoliation of graphene using aliphatic compounds: a supramolecular approach *Angew. Chem., Int. Ed.* **53** 10355–61
[39] Haar S *et al* 2014 A supramolecular strategy to leverage the liquid-phase exfoliation of graphene in the presence of surfactants: unraveling the role of the length of fatty acids *Small* **11** 1691–702
[40] Parvez K, Wu Z-S, Li R, Liu X, Graf R, Feng X and Müllen K 2014 Exfoliation of graphite into graphene in aqueous solutions of inorganic salts *J. Am. Chem. Soc.* **136** 6083–91
[41] Haar S, El Gemayel M, Shin Y, Melinte G, Squillaci M A, Ersen O, Casiraghi C, Ciesielski A and Samorì P 2015 Enhancing the liquid-phase exfoliation of graphene in organic solvents upon addition of n-octylbenzene *Sci. Rep.* **5** 16684
[42] Ciesielski A and Samori P 2014 Graphene via sonication assisted liquid-phase exfoliation *Chem. Soc. Rev.* **43** 381–98
[43] Parvez K, Yang S, Feng X and Müllen K 2015 Exfoliation of graphene via wet chemical routes *Synth. Met.* **210** 123–32
[44] Bonaccorso F, Bartolotta A, Coleman J N and Backes C 2016 2D-crystal-based functional inks *Adv. Mater.* **28** 6136–66
[45] Ciesielski A and Samorì P 2016 Supramolecular approaches to graphene: from self-assembly to molecule-assisted liquid-phase exfoliation *Adv. Mater.* **28** 6030–51
[46] Bellani S, Najafi L, Capasso A, Del Rio Castillo A E, Antognazza M R and Bonaccorso F 2017 Few-layer MoS_2 flakes as a hole-selective layer for solution-processed hybrid organic hydrogen-evolving photocathodes *J. Mater. Chem.* A **5** 4384–96
[47] Bellani S, Najafi L, Martín-García B, Ansaldo A, Del Rio Castillo A E, Prato M, Moreels I and Bonaccorso F 2017 Graphene-based hole-selective layers for high-efficiency, solution-processed, large-area, flexible, hydrogen-evolving organic photocathodes *J. Phys. Chem.* C **121** 21887–903
[48] Li D, Müller M B, Gilje S, Kaner R B and Wallace G G 2008 Processable aqueous dispersions of graphene nanosheets *Nat. Nanotechnol.* **3** 101
[49] Casaluci S, Gemmi M, Pellegrini V, Di Carlo A and Bonaccorso F 2016 Graphene-based large area dye-sensitized solar cell modules *Nanoscale* **8** 5368–78
[50] Secor E B, Prabhumirashi P L, Puntambekar K, Geier M L and Hersam M C 2013 Inkjet printing of high conductivity, flexible graphene patterns *J. Phys. Chem. Lett.* **4** 1347–51
[51] Torrisi F *et al* 2012 Inkjet-printed graphene electronics *ACS Nano* **6** 2992–3006
[52] Secor Ethan B, Lim S, Zhang H, Frisbie C D, Francis Lorraine F and Hersam Mark C 2014 Gravure printing of graphene for large-area flexible electronics *Adv. Mater.* **26** 4533–8
[53] Capasso A, Del Rio Castillo A E, Sun H, Ansaldo A, Pellegrini V and Bonaccorso F 2015 Ink-jet printing of graphene for flexible electronics: an environmentally-friendly approach *Solid State Commun.* **224** 53–63
[54] Wang J T-W *et al* 2014 Low-temperature processed electron collection layers of graphene/TiO_2 nanocomposites in thin film perovskite solar cells *Nano Lett.* **14** 724–30
[55] Agresti A, Pescetelli S, Cinà L, Konios D, Kakavelakis G, Kymakis E and Carlo A D 2016 Efficiency and stability enhancement in perovskite solar cells by inserting lithium-neutralized graphene oxide as electron transporting layer *Adv. Funct. Mater.* **26** 2686–94
[56] Zhu Z *et al* 2014 Efficiency enhancement of perovskite solar cells through fast electron extraction: the role of graphene quantum dots *J. Am. Chem. Soc.* **136** 3760–3
[57] Han G S, Song Y H, Jin Y U, Lee J-W, Park N-G, Kang B K, Lee J-K, Cho I S, Yoon D H and Jung H S 2015 Reduced graphene oxide/mesoporous TiO_2 nanocomposite based perovskite solar cells *ACS Appl. Mater. Interfaces* **7** 23521–6
[58] Agresti A, Pescetelli S, Taheri B, Del Rio Castillo A E, Cinà L, Bonaccorso F and Di Carlo A 2016 Graphene-perovskite solar cells exceed 18% efficiency: a stability study *ChemSusChem* **9** 2609–19
[59] Petridis C, Kakavelakis G and Kymakis E 2018 Renaissance of graphene-related materials in photovoltaics due to the emergence of metal halide perovskite solar cells *Energy Environ. Sci.* **11** 1030–61
[60] Del Rio Castillo A E *et al* 2018 High-yield production of 2D crystals by wet-jet milling *Mater. Horiz.* **5** 890–904
[61] Sun H *et al* 2016 Binder-free graphene as an advanced anode for lithium batteries *J. Mater. Chem.* A **4** 6886–95
[62] Yaghoobi Nia N, Zendehdel M, Cina L, Matteocci F and Di Carlo A 2018 A crystal engineering approach for scalable perovskite solar cells and module fabrication: a full out of glove box procedure *J. Mater. Chem.* A **6** 659–71
[63] Lee J-W, Lee T-Y, Yoo P J, Gratzel M, Mhaisalkar S and Park N-G 2014 Rutile TiO_2-based perovskite solar cells *J. Mater. Chem.* A **2** 9251–9
[64] Salim T, Sun S, Abe Y, Krishna A, Grimsdale A C and Lam Y M 2015 Perovskite-based solar cells: impact of morphology and device architecture on device performance *J. Mater. Chem.* A **3** 8943–69
[65] Chen D, Jordan E H and Gell M 2008 Porous TiO_2 coating using the solution precursor plasma spray process *Surf. Coat. Technol.* **202** 6113–9

[66] Kout A and Müller H 2009 Parameter optimization for spray coating *Adv. Eng. Softw.* **40** 1078–86
[67] Zhu Lifeng S J, Dongmei L and Qingbo M 2015 Effect of mesoporous TiO_2 layer thickness on the cell performance of perovskite solar cells *Acta Chim. Sin.* **73** 261–6
[68] Lee D G, Kim M-C, Kim B J, Kim D H, Lee S M, Choi M, Lee S and Jung H S 2017 Effect of TiO_2 particle size and layer thickness on mesoscopic perovskite solar cells *Appl. Surf. Sci.* (https://doi.org/10.1016/j.apsusc.2017.11.124)
[69] Hou X, Pan L, Huang S, Wei O-Y and Chen X 2017 Enhanced efficiency and stability of perovskite solar cells using porous hierarchical TiO_2 nanostructures of scattered distribution as scaffold *Electrochim. Acta* **236** 351–8
[70] Abdi-Jalebi M, Dar M I, Sadhanala A, Senanayak S P, Giordano F, Zakeeruddin S M, Grätzel M and Friend R H 2016 Impact of a mesoporous titania—perovskite interface on the performance of hybrid organic–inorganic perovskite solar cells *J. Phys. Chem. Lett.* **7** 3264–9
[71] Sun X, Xu J, Xiao L, Chen J, Zhang B, Yao J and Dai S 2017 Influence of the porosity of the TiO_2 film on the performance of the perovskite solar cell *Int. J. Photoenergy* **2017** 10
[72] Knorr F J, Mercado C C and McHale J L 2008 Trap-state distributions and carrier transport in pure and mixed-phase TiO_2: influence of contacting solvent and interphasial electron transfer *J. Phys. Chem.* C **112** 12786–94
[73] Zhang X, Wu Y, Huang Y, Zhou Z and Shen S 2016 Reduction of oxygen vacancy and enhanced efficiency of perovskite solar cell by doping fluorine into TiO_2 *J. Alloys Compd.* **681** 191–6
[74] Ng Y H, Lightcap I V, Goodwin K, Matsumura M and Kamat P V 2010 To what extent do graphene scaffolds improve the photovoltaic and photocatalytic response of TiO_2 nanostructured films? *J. Phys. Chem. Lett.* **1** 2222–7
[75] Im J-H, Jang I-H, Pellet N, Grätzel M and Park N-G 2014 Growth of $CH_3NH_3PbI_3$ cuboids with controlled size for high-efficiency perovskite solar cells *Nat. Nano* **9** 927–32
[76] Kumar M H *et al* 2014 Lead-free halide perovskite solar cells with high photocurrents realized through vacancy modulation *Adv. Mater.* **26** 7122–7
[77] Mallajosyula A T, Fernando K, Bhatt S, Singh A, Alphenaar B W, Blancon J-C, Nie W, Gupta G and Mohite A D 2016 Large-area hysteresis-free perovskite solar cells via temperature controlled doctor blading under ambient environment *Appl. Mater. Today* **3** 96–102
[78] Volonakis G and Giustino F 2015 Ferroelectric graphene-perovskite interfaces *J. Phys. Chem. Lett.* **6** 2496–502
[79] Katz E A, Mescheloff A, Visoly-Fisher I and Galagan Y 2016 Light intensity dependence of external quantum efficiency of fresh and degraded organic photovoltaics *Sol. Energy Mater. Sol. Cells* **144** 273–80
[80] Capasso A, Matteocci F, Najafi L, Prato M, Buha J, Cinà L, Pellegrini V, Carlo A D and Bonaccorso F 2016 Few-layer MoS_2 flakes as active buffer layer for stable perovskite solar cells *Adv. Energy Mater.* **6** 1600920
[81] Cacovich S, Cina L, Matteocci F, Divitini G, Midgley P A, Di Carlo A and Ducati C 2017 Gold and iodine diffusion in large area perovskite solar cells under illumination *Nanoscale* **9** 4700–6
[82] Biccari F *et al* 2017 Graphene-based electron transport layers in perovskite solar cells: a step-up for an efficient carrier collection *Adv. Energy Mater.* **7** 1701349
[83] Liang Y T, Vijayan B K, Gray K A and Hersam M C 2011 Minimizing graphene defects enhances titania nanocomposite-based photocatalytic reduction of CO_2 for improved solar fuel production *Nano Lett.* **11** 2865–70
[84] Halme J, Boschloo G, Hagfeldt A and Lund P 2008 Spectral characteristics of light harvesting, electron injection, and steady-state charge collection in pressed TiO_2 dye solar cells *J. Phys. Chem.* C **112** 5623–37
[85] Qiu L, Ono L K and Qi Y 2018 Advances and challenges to the commercialization of organic–inorganic halide perovskite solar cell technology *Mater. Today Energy* **7** 169–89
[86] Hwang I, Jeong I, Lee J, Ko M J and Yong K 2015 Enhancing stability of perovskite solar cells to moisture by the facile hydrophobic passivation *ACS Appl. Mater. Interfaces* **7** 17330–6
[87] Kim N-K *et al* 2017 Investigation of thermally induced degradation in $CH_3NH_3PbI_3$ perovskite solar cells using *in situ* synchrotron radiation analysis *Sci. Rep.* **7** 4645
[88] Jin J, Chen C, Li H, Cheng Y, Xu L, Dong B, Song H and Dai Q 2017 Enhanced performance and photostability of perovskite solar cells by introduction of fluorescent carbon dots *ACS Appl. Mater. Interfaces* **9** 14518–24
[89] Manga K K, Wang S, Jaiswal M, Bao Q and Loh K P 2010 High-gain graphene-titanium oxide photoconductor made from inkjet printable ionic solution *Adv. Mater.* **22** 5265–70
[90] Wen Y, Ding H and Shan Y 2011 Preparation and visible light photocatalytic activity of Ag/TiO_2/graphene nanocomposite *Nanoscale* **3** 4411–7
[91] Bell N J, Ng Y H, Du A, Coster H, Smith S C and Amal R 2011 Understanding the enhancement in photoelectrochemical properties of photocatalytically prepared TiO_2-reduced graphene oxide composite *J. Phys. Chem.* C **115** 6004–9
[92] Pathak S K *et al* 2014 Performance and stability enhancement of dye-sensitized and perovskite solar cells by Al doping of TiO_2 *Adv. Funct. Mater.* **24** 6046–55
[93] Ahn N, Kwak K, Jang M S, Yoon H, Lee B Y, Lee J-K, Pikhitsa P V, Byun J and Choi M 2016 Trapped charge-driven degradation of perovskite solar cells *Nat. Commun.* **7** 13422
[94] Busby Y, Agresti A, Pescetelli S, Di Carlo A, Noel C, Pireaux J-J and Houssiau L 2018 Aging effects in interface-engineered perovskite solar cells with 2D nanomaterials: A depth profile analysis *Mater. Today Energy* **9** 1–10
[95] Fan Z, Xiao H, Wang Y, Zhao Z, Lin Z, Cheng H-C, Lee S-J, Wang G, Feng Z, Goddard W A, Huang Y and Duan X 2017 Layer-by-layer degradation of methylammonium lead tri-iodide perovskite microplates *Joule* **1** 548–62